JACS Au
AN OPEN ACCESS JOURNAL OF THE AMERICAN CHEMICAL SOCIETY

pubs.acs.org/jacsau
Article

Plasma Chemical Looping: Unlocking High-Efficiency CO_2 Conversion to Clean CO at Mild Temperatures

Yanhui Long, Xingzi Wang, Hai Zhang,* Kaiyi Wang, Wee-Liat Ong, Annemie Bogaerts, Kongzhai Li, Chunqiang Lu, Xiaodong Li, Jianhua Yan,* Xin Tu,* and Hao Zhang*

Cite This: JACS Au 2024, 4, 2462−2473

ABSTRACT: We propose a plasma chemical looping CO_2 splitting (PCLCS) approach that enables highly efficient CO_2 conversion into O_2-free CO at mild temperatures. PCLCS achieves an impressive 84% CO_2 conversion and a 1.3 mmol g^{-1} CO yield, with no O_2 detected. Crucially, this strategy significantly lowers the temperature required for conventional chemical looping processes from 650 to 1000 °C to only 320 °C, demonstrating a robust synergy between plasma and the $Ce_{0.7}Zr_{0.3}O_2$ oxygen carrier (OC). Systematic experiments and density functional theory (DFT) calculations unveil the pivotal role of plasma in activating and partially decomposing CO_2, yielding a mixture of CO, O_2/O, and electronically/vibrationally excited CO_2*. Notably, these excited CO_2* species then efficiently decompose over the oxygen vacancies of the OCs, with a substantially reduced activation barrier (0.86 eV) compared to ground-state CO_2 (1.63 eV), contributing to the synergy. This work offers a promising and energy-efficient pathway for producing O_2-free CO from inert CO_2 through the tailored interplay of plasma and OCs.

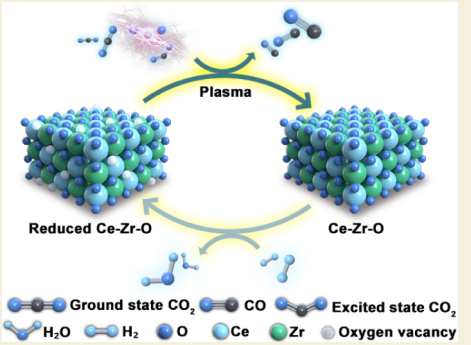

KEYWORDS: *gliding arc, chemical looping, CO_2 conversion, oxygen carrier*

INTRODUCTION

The escalating reliance on fossil fuels has led to a significant surge in anthropogenic carbon dioxide (CO_2) emissions, surpassing a record level of 410 ppm.[1] Confronted with this pressing environmental challenge, there is a compelling imperative to address and curtail CO_2 emissions by harnessing it as a valuable C1-feedstock through various chemical processes.[2,3] One such attractive process is the dissociation of CO_2 into carbon monoxide (CO), a pivotal industrial feedstock essential for the synthesis of various chemicals and fuels, including alcohols, liquid hydrocarbons, and organic acids.[4,5] This avenue of carbon utilization represents an appealing means to close the carbon loop, potentially opening up innovative avenues for the chemical industry.[4]

Nevertheless, owing to the linear structure and chemical inertia of CO_2, this reaction faces a formidable thermodynamic barrier ($CO_2 \rightarrow CO + 1/2\ O_2$, $\Delta H_{298\ K} = 280$ kJ mol^{-1}) in breaking the C=O bond (803 kJ mol^{-1}). Despite many advances and successful proof-of-concepts being reported, the activation of CO_2 for effective conversion remains a great challenge.[3,6−9] For thermal and photothermal processes, CO_2 splitting becomes favorable only at extremely elevated temperatures, with the reaction equilibrium strongly favoring the formation of reactants. Even at temperatures as high as 2000 K, the conversion of CO_2 reaches only 1.5%.[10−12] Electrochemical methods grapple with issues of low energetic efficiency (or large overpotential), and sluggish electron transfer kinetics.[13] Similarly, photochemical processes face limitations in terms of photon efficiency.[3] Nonthermal plasmas (NTPs) have recently emerged as a promising avenue for CO_2 conversion under mild condition, attributed to the abundance of reactive species (electrons, radicals, and excited species).[6,8,12,14] Moreover, plasma processes ensure rapid startup, high reaction rates, compactness, ease of installation, and flexibility. These attributes enable the direct utilization of electricity generated from intermittent renewable sources, offering a flexible solution for peak shaving and grid stabilization.[12] Nonetheless, challenges in conversion and energy efficiency constrain their potential application.[12]

Furthermore, the typically inevitable presence of O_2 in the gas products not only hinders CO_2 conversion, particularly due to recombination reactions at elevated gas temperatures, but also introduces the risk of catalyst deactivation.[11−13,15] For instance, electrocatalytic conditions with rapid electron collections typically have an O_2 tolerance of less than 2% v/v.[16] Certainly, the necessity for an expensive gas separation/purification

Received: February 19, 2024
Revised: April 15, 2024
Accepted: April 25, 2024
Published: May 8, 2024

process to eliminate O_2 impurities represents another significant challenge.[17]

To address the above challenges, we propose a novel plasma chemical looping CO_2 splitting (PCLCS) approach to efficiently convert CO_2 into O_2-free CO. This approach, integrating a custom-built rotating gliding arc (RGA) plasma with a reduced oxygen carrier (OC), harnesses the strong activation capabilities of plasma on inert CO_2 molecules[6] and the distinctive oxygen-carrying capacity of OCs for effective CO_2 reduction.[18] The RGA provides a stable "warm" plasma with a high energy density and allows for instant on/off for the initial activation and partial composition of CO_2. Significantly, compared to conventional NTPs such as dielectric barrier discharge (DBD), the energy distribution within RGA stimulates the most efficient CO_2 decomposition route via vibrational excitation. Zirconium-doped ceria ($Ce_xZr_{1-x}O_2$, x = 0.1−0.5) forming a Ce−Zr−O solid solution was developed as the OC. Compared to other typical OCs (e.g., Fe-based, Mn-based), ceria is particularly attractive owing to its rapid redox kinetics and robust structural and crystallographic stability.[18] In addition, the addition of Zr^{4+} into CeO_2 could considerably enhance the surface/bulk oxygen mobility and reactivity by introducing crystallographic defects.[19]

The efficacy of the PCLCS system was appraised over $Ce_xZr_{1-x}O_2$ with varying Zr contents, and a comprehensive examination of the physicochemical characteristics of the OCs was undertaken. Notably, achieving a CO_2 conversion of up to 84% and a CO yield of 1.3 mmol g^{-1}, devoid of detectable O_2, at mild temperature of only 320 °C in the OC region highlights a robust synergy between plasma and the OC. The intricate interplay between the plasma and the OC was meticulously elucidated through a synergistic combination of extensive experimental analyses and molecular scale density functional theory (DFT) calculations. The decisive contribution of excited CO_2*, generated by the plasma, and its interactions with the oxygen vacancies of the OC were convincingly demonstrated as a pivotal factor driving the observed synergy.

RESULTS AND DISCUSSION

Performance of PCLCS

The PCLCS setup comprising a custom-built RGA reactor and a quartz cover housing the OCs is illustrated in Figure 1. Further

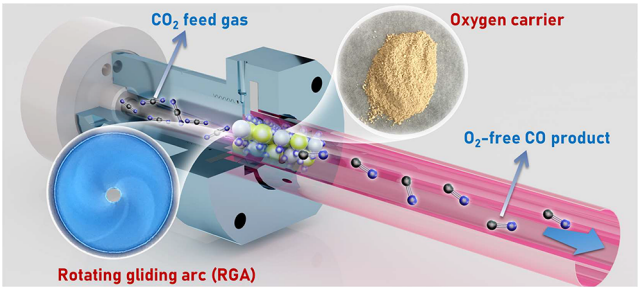

Figure 1. Schematic of the Plasma Chemical Looping CO_2 Splitting (PCLCS) setup.

information on the setup configuration and the experimental system is presented in Figures S1 and S2 of Section S1. PCLCS experiments were conducted at a weight hourly space velocity (WHSV) of 300,000 $cm^3\ g^{-1}\ h^{-1}$ without external heating.

The time-resolved CO concentrations in the products, as well as the CO_2 conversion and CO yield of PCLCS using different $Ce_{1-x}Zr_xO_{2-\delta}$ OCs, are plotted in Figure 2. More detailed concentration profiles are provided in Figures S3 and S4. For Zr-doped OCs, CO is immediately produced upon plasma activation, reaching its maximum concentration within only 5 to 20 s, maintaining for approximately 110−140 s, and followed by a rapid decline to zero due to the oxidation of the OCs. $CeO_{2-\delta}$ exhibits a significantly lower reaction rate, as indicated by the low CO concentration and its slow initial increase rate. Interestingly, no O_2 was detected in the gas products.

Incorporating Zr into CeO_2 significantly enhances the reaction performance, with effects varying depending on the doping ratio. Figure 2a,b, shows a consistent improvement in both the CO concentration (and yield) and the CO_2 conversion as the Zr content increases from 0% to 30%. $Ce_{0.7}Zr_{0.3}O_{2-\delta}$, in particular, achieves the highest CO_2 conversion (up to ∼84%), a substantial increase compared to the limited CO_2 conversion of $CeO_{2-\delta}$ (12%). Consequently, $Ce_{0.7}Zr_{0.3}O_{2-\delta}$ attains a maximum CO yield of 1.3 mmol g^{-1}, surpassing the yield of $CeO_{2-\delta}$ by a factor of around seven. However, a further increase in the Zr content to 50% leads to a significant decline in reaction performance. These trends align well with the OC characterization results in Table 1, namely that the oxygen vacancy abundance of the OCs reaches a maximum at a Zr content of 30%, followed by a remarkable drop as the Zr content further increases to 50%. Based on these results, $Ce_{0.7}Zr_{0.3}O_{2-\delta}$ was chosen as the OC for subsequent experiments.

Importantly, these results were achieved at a mild reaction temperature of only 320 °C on the OCs, as measured by the thermocouple. To elucidate the specific role of plasma in CO_2 conversion in PCLCS, thermal chemical looping (CL) CO_2 splitting experiments over reduced $Ce_{0.7}Zr_{0.3}O_{2-\delta}$ were comparatively performed in a tube furnace at the same temperature of 320 °C. Figure 2c−f presents a comparison of the time-resolved product composition, CO yield, and CO_2 conversion between thermal CL experiments and PCLCS. Additionally, we compare the performance of PCLCS with typical CO_2 splitting results reported in literature for NTP and thermal CL processes.

As shown in Figure 2c,d, the thermal CL method fails to reduce CO_2 at such a mild temperature of 320 °C. In contrast, PCLCS, aided by plasma without additional heating, achieves a remarkable CO_2 conversion of up to 84% and a CO yield of 1.3 mmol g^{-1}. The CO_2 temperature program oxidation (CO_2-TPO) results presented in Figure S5 reveal that thermal CL CO_2 splitting is initiated only at above 400 °C. A further comparison with state-of-the-art literature results (Figure 2e) shows that PCLCS dramatically reduces the required reaction temperature compared to thermal CL from 650 to 1000 to 320 °C, with comparable or only slightly lower CO_2 conversion. Moreover, PCLCS achieves significantly higher CO_2 conversion (∼84%) compared to typical NTP sources in the literature (only 4%−50%), as shown in Figure 2f. The energy efficiency of PCLCS (6.4% to 18.2%, refer to Table S1) is comparable or superior to that of DBD plasmas (typically <10%), although slightly lower than that of gliding arc (GA) or other warm plasmas (typically <35%).[12] Nonetheless, further enhancement is anticipated through the utilization of more OCs or optimization of the reaction conditions, as suggested by the results in Table S1. Note that no O_2 was detected in the products of our PCLCS system, while in NTP processes, an O_2 concentration of half that of CO is typically reported.[12,33]

The above results suggest that PCLCS provides a strong synergy between plasma and OCs in facilitating the kinetics of CO_2 splitting, achieving high CO_2 conversion (∼84%), and an O_2-free CO product (1.3 mmol g^{-1}), at a mild temperature of

https://doi.org/10.1021/jacsau.4c00153
JACS Au 2024, 4, 2462−2473

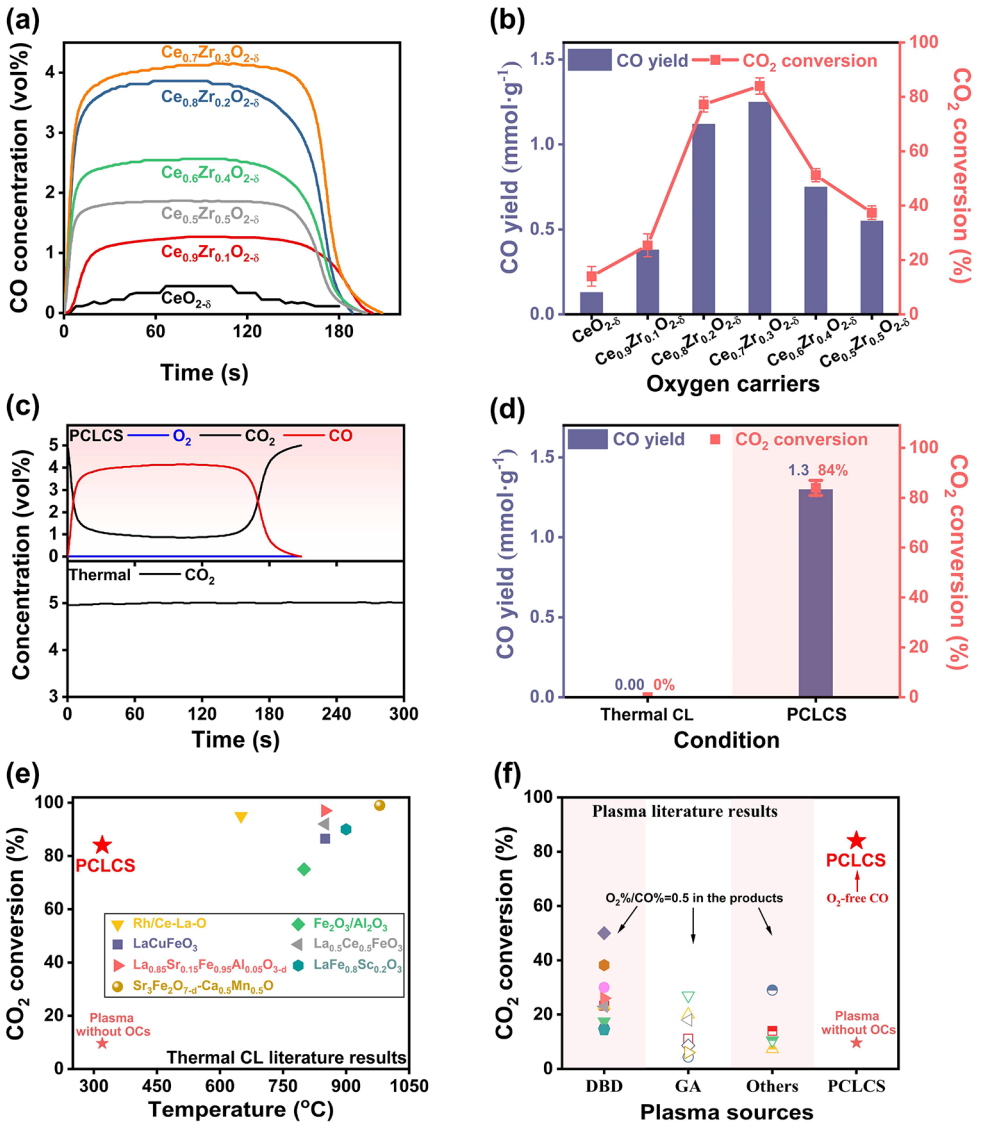

Figure 2. Performance of PCLCS. (a) Time-resolved concentrations of CO and (b) CO_2 conversion and CO yield over $Ce_{1-x}Zr_xO_{2-\delta}$ (x = 0, 0.1, 0.2, 0.3, 0.4, and 0.5). Comparison of PCLCS (over reduced $Ce_{0.7}Zr_{0.3}O_{2-\delta}$) and thermal chemical looping (CL) at 320 °C: (c) Time-resolved product composition, (d) CO yield and CO_2 conversion, and (e) CO_2 conversion with respect to the reaction temperature among PCLCS and state-of-the-art thermal CL CO_2 splitting works.[20−26] (f) CO_2 conversion among PCLCS and state-of-the-art NTP for CO_2 splitting.[6,7,27−45]

Table 1. XPS-Derived Characteristics of $Ce_{1-x}Zr_xO_{2(-\delta)}$ OCs

oxygen carriers		oxygen species percentage (%)				Ce ion percentage (%)		
		O I	O II	O III	O_{ads}/O_{latt} ratio	Ce^{3+}	Ce^{4+}	Ce^{3+}/Ce^{4+} ratio
fresh	CeO_2	58	38	4	0.72	11.97	88.02	0.14
	$Ce_{0.9}Zr_{0.1}O_2$	48	41	11	1.08	14.62	85.38	0.17
	$Ce_{0.8}Zr_{0.2}O_2$	40	28	32	1.50	15.85	84.15	0.19
	$Ce_{0.7}Zr_{0.3}O_2$	27	61	12	2.70	21.14	78.86	0.27
	$Ce_{0.6}Zr_{0.4}O_2$	41	43	16	1.44	13.52	86.48	0.16
	$Ce_{0.5}Zr_{0.5}O_2$	55	35	10	0.82	11.17	88.83	0.13
reduced	$CeO_{2-\delta}$	28	62	10	2.57	13.97	86.03	0.16
	$Ce_{0.7}Zr_{0.3}O_{2-\delta}$	10	86	4	9.00	34.67	65.33	0.53
oxidized	CeO_2	57	37	6	0.75	11.02	88.98	0.12
	$Ce_{0.7}Zr_{0.3}O_2$	24	67	9	2.03	20.80	79.20	0.26

only 320 °C. It should be noted that the oxidized OC requires reduction at a relatively high temperature in a tube furnace (800 °C under H_2 in this work). However, there are avenues for lowering the reaction temperature. For instance, modifying Ce-based OCs with trace amounts of metals such as Rh and Ni, or utilizing Mo-based OCs, as demonstrated in previous literature,[20,46,47] have shown promise in reducing the required reaction temperature.

https://doi.org/10.1021/jacsau.4c00153
JACS Au 2024, 4, 2462−2473

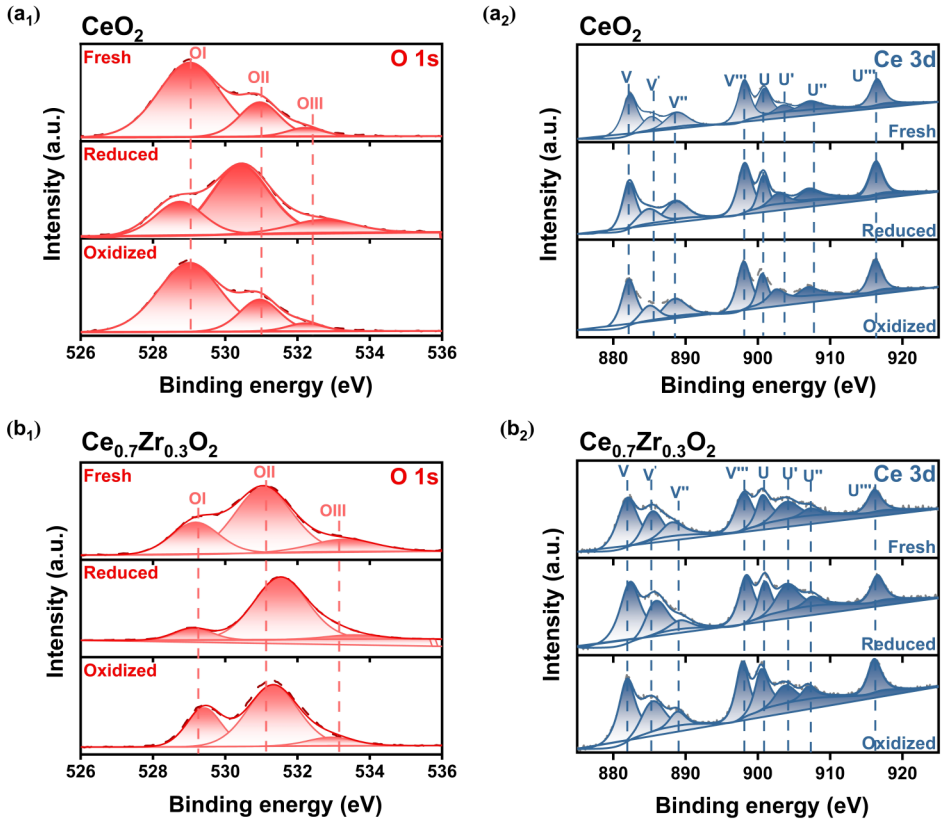

Figure 3. XPS results. XPS spectra for O 1s and Ce 3d over (a) CeO_2 and (b) $Ce_{0.7}Zr_{0.3}O_2$ at various stages (fresh, reduced, and oxidized).

The stability of the PCLCS system and the OCs was further assessed through 10 redox cycle tests. Results in Figure S5 show that the CO yield and CO_2 conversion remained consistently high, around 1.3 mmol g^{-1} and 82−84%, respectively, throughout the cycles. The minimal degradation, only approximately 0.038% per cycle, demonstrated excellent redox stability. Moreover, the CO purity in the products remained almost 100%, with no detectable presence of O_2. The physicochemical characteristics of the $Ce_{0.7}Zr_{0.3}O_2$ OCs before (fresh) and after (cycled) the redox cycle are presented in Figures S7 and S8. The X-ray diffraction (XRD) patterns in Figure S7a confirm that both the fresh and cycled samples exhibit crystal structures consistent with the standard fluorite type cubic phase of CeO_2 (JCPDS card [43−1002]). The H_2-temperature programmed reduction (H_2-TPR) profile of the cycled $Ce_{0.7}Zr_{0.3}O_2$ in Figure S7b closely resembles that of the fresh sample, indicating complete restoration of the crystallite state after the redox cycle. Scanning electron microscopy (SEM) and transmission electronmicroscopy (TEM) images in Figures S7c,d and S8 depict that the Zr element region almost coincides with the Ce element regions in the fresh sample, suggesting a uniform dispersion of Zr cations in the CeO_2 lattice (Figure S7d). After cycling, all elements exhibit a similar distribution with no detectable agglomeration of Zr or other elements. In addition, the SEM images show only a negligible increase in the particle size for the cycled sample. All these observations collectively indicate that the microstructure of $Ce_{0.7}Zr_{0.3}O_2$ OCs remains stable during the redox cycles, substantially contributing to the high stability of PCLCS for O_2-free CO production from CO_2.

Physicochemical Characteristics of the OCs: Effect of Zr Doping

To unravel the underlying mechanisms of PCLCS and comprehend the distinct performance exhibited by various OCs, we conducted a comprehensive examination of the physicochemical characteristics of $Ce_{1-x}Zr_xO_2$, highlighting the impact of Zr doping. Moreover, DFT calculations were performed to gain insight into the effects at an atomic level.

The XRD patterns of the freshly synthesized $Ce_{1-x}Zr_xO_2$ (x = 0, 0.1, 0.2, 0.3, 0.4, 0.5) OCs are presented in Figure S9, revealing that the crystal structures of all samples match well the face-centered cubic (fcc) fluorite structure of CeO_2, with no detectable impurity phases, except in the case of $Ce_{0.5}Zr_{0.5}O_2$ (Figure S9a). The enlarged portion of single CeO_2 in Figure S9b shows that the diffraction peaks of CeO_2 (111) in Zr-containing samples shift slightly toward higher diffraction angles, accompanied by peak broadening. To scrutinize the structural changes in the fluorite structure after Zr doping, Rietveld refinement calculations were performed on the XRD patterns of CeO_2 and $Ce_{0.7}Zr_{0.3}O_2$ samples, as an example, as presented in Figure S9c,d and summarized in Table S2. The table summarizes that the R_{wp} value for both samples is below 10%, and the χ^2 value is around 3.0, indicating the high reliability of the refined results due to the good match between the theoretical model and the test data. It can be inferred that Zr doping in the CeO_2 lattice is achieved by replacing some of Ce^{4+}. In this case, the cell parameters (a, b, and c) of $Ce_{0.7}Zr_{0.3}O_2$ are slightly smaller than those of CeO_2 due to the smaller Zr^{4+} radius (0.08 nm) compared to Ce^{4+} (0.092 nm). The results suggest that the Zr ions are incorporated into the CeO_2 lattice to form a Ce−Zr−O solid solution.

https://doi.org/10.1021/jacsau.4c00153
JACS Au 2024, 4, 2462−2473

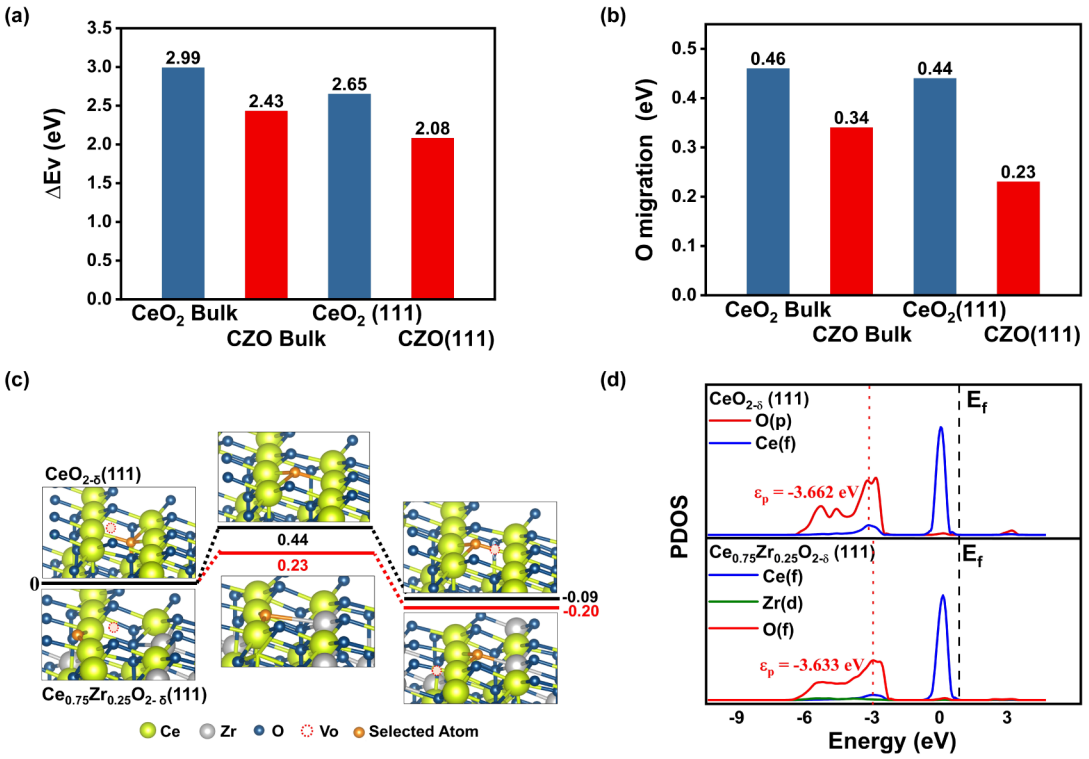

Figure 4. Effect of Zr doping. (a) Computed energies of oxygen vacancy formation (ΔE_V) and (b) Energy barriers of oxygen vacancy migration, for bulk and (111) surface of CeO_2 and $Ce_{0.7}Zr_{0.3}O_2$ (CZO). (c) Energy potential profile along the most favorable oxygen migration pathway on the (111) surfaces of CeO_2 and $Ce_{0.7}Zr_{0.3}O_2$ (CZO). (d) Electronic projected density of states (PDOS) of $CeO_{2-\delta}$ and $Ce_{0.7}Zr_{0.3}O_{2-\delta}$.

H_2-TPR experiments were conducted to assess the oxygen mobility of $Ce_{1-x}Zr_xO_2$. As depicted in Figure S10, CeO_2 exhibits two distinct reduction peaks, with the first spanning 490 to 600 °C, and the second consistently rising after 700 °C.[19,48,49] The low-temperature peak can be attributed to the consumption of surface oxygen species on CeO_2, while the high temperature peak involves the consumption of bulk lattice oxygen and the reduction of Ce^{4+} to Ce^{3+}. Increasing Zr content (x = 0.1, 0.2, 0.3, 0.4) shifts the second peak to lower temperatures and the first peak to higher temperatures, forming a larger peak. This shift indicates simultaneous surface and bulk reduction. As surface oxygen is consumed, bulk oxygen rapidly migrates to replenish the depleted surface oxygen, reflecting the reducibility and mobility of lattice oxygen.[50,51] These results indicate that Zr introduction into CeO_2 enhances lattice oxygen reduction at lower temperatures, indicating significantly improved lattice oxygen mobility. Among these six samples, $Ce_{0.7}Zr_{0.3}O_2$ exhibits the largest peak area and highest H_2 consumption, suggesting that 30% Zr doping is optimal for achieving a desired balance between active CeO_2 and inert ZrO_2.

To elucidate the surface elemental composition and chemical status of the OCs in various states, X-ray photoelectron spectroscopy (XPS) characterization was conducted on freshly prepared $Ce_{1-x}Zr_xO_2$ (labeled as "fresh") with different Zr contents (x = 0, 0.1, 0.2, 0.3, 0.4, 0.5). The corresponding spectra are presented in Figure S11. Additionally, CeO_2 and $Ce_{0.7}Zr_{0.3}O_2$, used in our PCLCS experiments, was characterized at different stages: 1) fresh; 2) reduced before use in PCLCS (labeled as "reduced"); and 3) oxidized after use in PCLCS (labeled as "oxidized"), with the spectra illustrated in Figure 3. In the O 1s spectrum (Figures S11a and 3a), the predominant peak at 529.5 eV (labeled as O I) corresponds to lattice oxygen (O_{latt}), while the minor peaks at 531.8 eV (labeled as O II) and 533.2 eV (labeled as O III) likely represent low coordination surface-absorbed oxygen species (O_{ads}, e.g., hydroxyl and carbonate species).[52−54] In the Ce 3d spectrum (Figures S11b and 3b), V (V, V′, V″, and V‴) peaks correspond to Ce $3d_{5/2}$, and U (U, U′, U″, and U‴) peaks represent Ce $3d_{3/2}$. The V−U, V″−U″, and V‴−U‴ doublets indicate Ce (IV) final states (Ce^{4+} ions), while V′ and U′ peaks suggest Ce^{3+} ions.[54,55] The atomic molar ratios of the surface species across different samples, calculated based on the fitted peaks, are tabulated in Table 1. Considering that Brunauer−Emmett−Teller (BET) characterization shows no notable difference in the specific surface area for different OCs (e.g., CeO_2: 36.6 $m^2\ g^{-1}$ vs $Ce_{0.7}Zr_{0.3}O_2$: 37.3 $m^2\ g^{-1}$), the concentration of oxygen vacancies in OCs can be considered as proportional to the O_{ads}/O_{latt} ratio.[54,56] Zr to CeO_2 enhances the O_{ads}/O_{latt} ratio, as summarized in Table 1. Nevertheless, after reaching a maximum for $Ce_{0.7}Zr_{0.3}O_2$ (2.70), the ratio of the O_{ads}/O_{latt} then drops with further rising Zr content from x = 0.3 to 0.5. This indicates that adding an appropriate amount of Zr enhances the formation of oxygen vacancies, likely due to the chemical interactions between ZrO_2 and CeO_2. Consistently, Table 1 summarizes that the introduction of Zr^{4+} increases the Ce^{3+}/Ce^{4+} ratio in $Ce_{1-x}Zr_xO_2$, inducing the formation of oxygen vacancies. Again, $Ce_{0.7}Zr_{0.3}O_2$ exhibited the highest Ce^{3+} concentration, implying the most abundant oxygen vacancies. For higher Zr content ($x \geq$ 0.4), the reduced oxygen vacancy concentration in $Ce_{0.6}Zr_{0.4}O_2$ and $Ce_{0.5}Zr_{0.5}O_2$ is likely attributed to the ZrO_2 agglomeration on the material and the limited solid solution content (as observed in the XRD patterns in Figure S9).[57]

The H_2-TPR and XPS results reveal that $Ce_{0.7}Zr_{0.3}O_2$ possesses the most abundant oxygen vacancies, aligning well with the experimental findings (see Figure 2a,b) where $Ce_{0.7}Zr_{0.3}O_2$ demonstrated the highest CO yield and CO_2

https://doi.org/10.1021/jacsau.4c00153
JACS Au 2024, 4, 2462−2473

conversion. This underscores the pivotal role of oxygen vacancy abundance in PCLCS. Additionally, the characterization results for CeO_2 and $Ce_{0.7}Zr_{0.3}O_2$ at different stages in Table 1 indicate that reducing the OCs significantly improves the oxygen vacancies, with the reduced $Ce_{0.7}Zr_{0.3}O_{2-\delta}$ showing remarkably higher abundance. This contributes significantly to the efficient conversion of CO_2 in PCLCS. Above all, the concentration of oxygen vacancies plays a virtual role in the PCLCS process.

To elucidate the role of Zr in a Ce−Zr−O solid solution at an atomic level, DFT calculations were conducted to determine (i) the bulk and surface oxygen vacancy formation energies (ΔE_V) and (ii) the energy barrier for oxygen vacancy migration in both pure and Zr-doped ceria (CeO_2 and $Ce_{0.7}Zr_{0.3}O_2$, respectively). The former quantifies the thermodynamic energy required for lattice oxygen removal, and the latter depicts the ease of vacancy migration from a kinetics viewpoint. Both are crucial factors for the oxygen conductivity that is required for macroscopic lattice oxygen removal and redeposition in redox reactions. Moreover, Bader charge of CeO_2 and $Ce_{0.7}Zr_{0.3}O_2$ that refer to the simulated valence electron and electronic projected density of states (PDOS) of $CeO_{2-\delta}$ and $Ce_{0.7}Zr_{0.3}O_{2-\delta}$ were studied to further illustrate the bonding ability between certain surface atoms of the substrate. The computational details are provided in Section S2.

In the construction of the $Ce_{0.7}Zr_{0.3}O_2$ unit cell, two Ce atoms in the pristine CeO_2 unit cell were replaced by Zr atoms, and then, one O atom was removed to form an oxygen vacancy. These model structure details are presented in Section S2.1. The main DFT calculation results are presented in Figure 4.

The computed bulk oxygen vacancy formation energy (ΔE_V) for $Ce_{0.7}Zr_{0.3}O_2$ was found to be 2.43 eV (Figure 4a), notably lower than that for pristine CeO_2 (2.99 eV.[58] Additionally, the ease of O migration in $Ce_{0.7}Zr_{0.3}O_2$ bulk can be correlated with a lower barrier of 0.34 eV compared to 0.46 eV for pure CeO_2[59] (Figure 4b), as computed through transition-state calculations. For vacancy creation and migration on the surface, the (111) surface was selected for both CeO_2 and $Ce_{0.7}Zr_{0.3}O_2$ since it is reported to be the most stable ceria surface.[20,60] Indeed, many studies indicate that doping with various elements can substantially modify the surface properties of CeO_2.[19,20,59,61] A smaller ΔE_V of 2.08 eV (Figure 4a) was computed for the $Ce_{0.7}Zr_{0.3}O_2$ (111) surface than for the $Ce_{0.7}Zr_{0.3}O_2$ bulk (2.43 eV) (Figure 4a), indicating a higher surface oxygen vacancy concentration than the initially assumed $Ce_{0.7}Zr_{0.3}O_2$ stoichiometry. The migration pathway of the subsurface oxygen to the vacancy site has a very low barrier of 0.23 eV, which is much lower than that of the CeO_2 (111) surface (0.44 eV) (Figure 4c). More detailed calculation methods and results about oxygen formation energy and migration barrier calculations of CeO_2 and $Ce_{0.75}Zr_{0.25}O_{2-\delta}$ (111) surface or bulk are presented in Section S2.1 and Section S2.2.

Overall, the DFT results indicate significantly easier oxygen migration and release in Zr-doped ceria. The doping of Zr can effectively reduce the electron donation by the cations compared to CeO_2, thereby decreasing the number of valence electrons on oxygen anions (from 1.22 $^{e-}$ per O for pristine ceria to 1.20 $^{e-}$ according to the Bader charge analysis results). The reduction in electron density weakens the strength of the metal−oxygen (M-O) ionic bond. This effect of Zr substitution, combined with existing oxygen vacancies, reorganizes the electronic states in $Ce_{0.7}Zr_{0.3}O_2$ compared to those in CeO_2. Such a reorganization of oxygen electronic states can be well described by the oxygen p-band center (ε_p), which is related to the hybridization of metal and oxygen orbitals and has been used as an effective descriptor of the activity of lattice oxygen. Figure 4d shows an upward shift of ε_p after Zr doping, indicating stronger coupling between the electronic orbitals of oxygen and metal atoms. This enhanced coupling contributes to the higher activity of lattice oxygen in $Ce_{0.7}Zr_{0.3}O_2$, making Zr doping an effective strategy to improve the redox performance of ceria by reducing the energy barriers for both oxygen vacancy formation and migration.

Synergy Between Plasma and OC

In this section, we investigate the underlying synergy mechanisms through a combination of experiments and theoretical calculations. In the plasma-OC tandem system, the reactant CO_2 initially traverses the plasma region and subsequently interacts with the OCs. The plasma, generating highly energetic electrons and excited species, activates and partially splits CO_2, as previously reported.[6,11,62] This process produces excited CO_2*, besides ground-state CO_2, as well as CO, O_2, and O radicals, which undergo further CO_2 conversion and O_2/O removal on the OC, facilitated by the abundance of oxygen vacancies.

To gain insights into the reactions occurring in these two stages (ground stage and excited stage), we measured the intermediate gas products after the plasma (before the OC) utilizing a meticulously designed in situ gas sampling setup positioned between the plasma and the OC. This sampling setup allows for "freezing" the chemical composition of the sampled plasma gas products, thereby minimizing secondary reactions during sampling. Details of the sampling setup are schematically shown in Figure S12 with accompanying descriptions. The results revealed that CO_2 (5 vol%, in Ar) was converted into a mixture of 4.4 vol% CO_2, 0.6 vol% CO, and 0.3 vol% O_2 (in Ar) by plasma, resulting in a 14% CO_2 conversion. On the OCs, further reactions led to a gas composition of, for instance, 0.9 vol % CO_2, 4.1 vol% CO, and 0.0 vol% O_2 (in Ar) in the case of $Ce_{0.7}Zr_{0.3}O_{2-\delta}$, achieving a total CO_2 conversion of up to 84%.

To understand whether the role of plasma in PCLCS is exclusively the production of a CO_2/CO/O_2/O gas mixture, which is potentially more efficiently reduced on subsequent OCs compared to pure CO_2, we conducted additional thermal CL tests employing the intermediate gas composition (4.4 vol% CO_2, 0.6 vol% CO, 0.3 vol% O_2, in Ar) in a tube furnace over reduced $Ce_{0.7}Zr_{0.3}O_{2-\delta}$ at the same temperature of 320 °C as the PCLCS system. The time-resolved gas composition results, depicted in Figure S13, indicate effective O_2 capture by the reduced $Ce_{0.7}Zr_{0.3}O_{2-\delta}$ at this temperature. However, no conversion of CO_2 to CO is observed over the OC for the intermediate gas composition, suggesting the presence of additional synergistic effects between the plasma and the OC.

Plasma has proven the ability of modifying the physicochemical properties of catalysts, influencing the kinetics of chemical reactions, as previously reported.[12,63] To investigate whether such modifications occur in the context of PCLCS, the impact of plasma treatment (Ar as the carrier gas) on the chemical status of reduced $Ce_{0.7}Zr_{0.3}O_2$ was evaluated through XPS analysis. The results presented in Figure S14 indicate negligible changes in the surface valence states of $Ce_{0.7}Zr_{0.3}O_2$ before and after plasma treatment. This observation aligns logically with the experimental setup, where a distance of 2 mm between the OCs and the plasma in the PCLCS system in principle contributes to negligible alterations in the surface chemistry.

The above findings imply that the synergy between plasma and OC in PCLCS must be linked to the plasma composition

https://doi.org/10.1021/jacsau.4c00153
JACS Au 2024, 4, 2462−2473

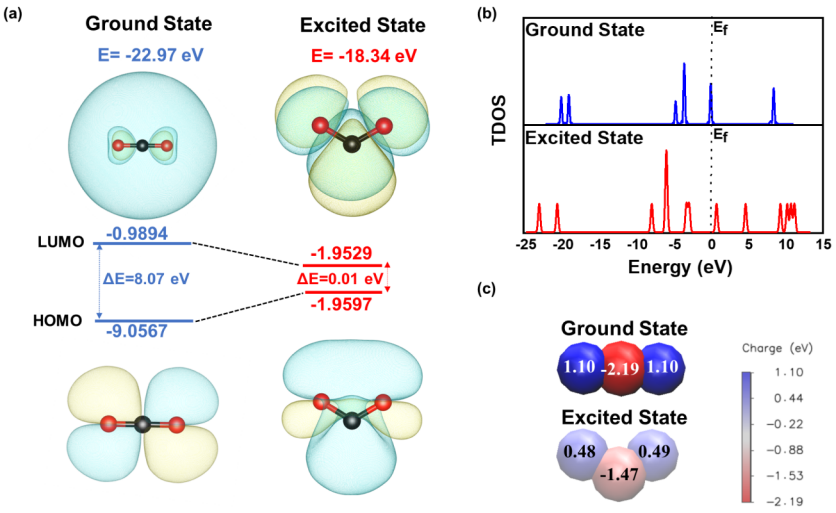

Figure 5. Elucidating different states of CO_2. (a) HOMO and LUMO of CO_2 in the ground state and excited state, (b) TDOS of CO_2 in the ground state and excited state, and (c) Bader charge analysis of CO_2 in the ground state and excited state.

and is likely attributed to the generation of excited CO_2* molecules within the plasma, which subsequently undergo further splitting on the OCs to yield CO. The fraction of electron energy transferred to different channels of CO_2 excitation and ionization in plasma was thus calculated, as a function of the reduced electric field (E/n) for the investigated 95 vol% Ar + 5 vol% CO_2 gas mixture, from the corresponding cross-sections of the electron impact reactions, by using the electron Boltzmann equation solver BOLSIG+.[64] The results, presented in Figure S15, suggest the abundance of both electronically and vibrationally excited CO_2* molecules in the RGA plasma with an E/n range of 21−25 Td.

For CeO_2-based OCs, oxygen vacancies are recognized as potent surface sites for the reactant adsorption and subsequent activation. Moreover, the formation of oxygen vacancies creates pathways for oxygen transport through the bulk lattice for surface reactions.[54] In a typical CO_2 splitting reaction over OC, CO_2 molecules are adsorbed on the sites of either surface vacancies and activated into carbonate intermediates. Simultaneously, carbonates undergo rapid splitting into CO and O atoms, which either exchange with oxygen vacancies on the surface or migrate into the bulk crystal to recharge the Ce^{3+} cations in the OCs, benefiting from excellent mobility of lattice oxygen.[57]

DFT calculations were further conducted to elucidate the difference between excited and ground state CO_2 over reduced $Ce_{0.7}Zr_{0.3}O_{2-\delta}$ in the above process. The electronic state of CO_2 excitation in the gas phase was constructed by electron relocation from the highest occupied molecular orbital (HOMO) to the lowest unoccupied molecular orbital (LUMO) of the ground-state CO_2.[65] As illustrated in Figure 5a, after fixing the occupation of the electronic state, a structural distortion with a bending geometry occurs, along with a total energy increase of −22.97 eV toward −18.34 eV, signifying a less stable molecular structure. It should be noted that a similar bending excited state CO_2 was also reported experimentally.[66] Simultaneously, the LUMO energy significantly decreased from −9.06 eV to −1.96 eV and the HOMO−LUMO gap shrank from −8.07 eV to −0.01 eV before and after excitation. This makes it easier for the frontier electron to transfer from the occupied antibonding orbital σ* to the unoccupied π* orbit, indicating that the molecule tends to be easily activated during the reaction process.[67]

The total density of states (TDOS) of the ground-state and excited-state CO_2, shown in Figure 5b, confirms this phenomenon: the LUMO of the excited state splits into two, resulting in the occupation of lower energy nondegenerate orbits.[68] The Bader charge analysis, presented in Figure 5c, shows that a −0.50 eV charge is transferred to the vacuum charge after excitation, reconfirming a more active intermediate CO_2 that reacts over $Ce_{0.7}Zr_{0.3}O_{2-\delta}$.

The potential energy pathway of CO_2 splitting on the $Ce_{0.7}Zr_{0.3}O_{2-\delta}$ (111) surface is presented in Figure 6, and more

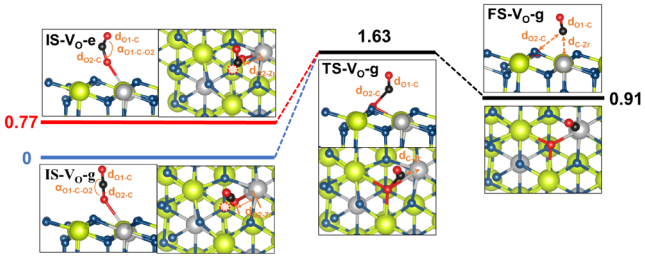

Figure 6. DFT calculations of different states of CO_2 splitting on $Ce_{0.7}Zr_{0.3}O_{2-\delta}$. Potential energy pathway of CO_2* → CO+O on $Ce_{0.7}Zr_{0.3}O_{2-\delta}$ (111) surface, where "e" represents the excited-state CO_2* and "g" denotes the ground-state CO_2.

details are shown in Section S2.3. The calculation results show that the reaction involving excited CO_2* exhibits a considerably lower activation barrier (0.86 eV), almost half of that associated with the ground state of CO_2 (1.63 eV). Additionally, the reaction energy drops remarkably from 0.91 to 0.14 eV. These findings suggest that plasma-excited CO_2* is significantly more reactive over the oxygen vacancies of $Ce_{0.7}Zr_{0.3}O_{2-\delta}$ compared to the ground-state CO_2 for splitting reactions.

The above investigation and analyses enable us to propose the underlying mechanism of the synergy between plasma and OCs, as schematically shown in Figure 7. 1) Plasma rapidly elevates the mixture temperature through energy transfer from electrons to neutral molecules, providing a temperature of around 320 °C for the thermal reactions over the OCs, eliminating the need for an external heat source. 2) Plasma initiates the activation and

https://doi.org/10.1021/jacsau.4c00153
JACS Au 2024, 4, 2462−2473

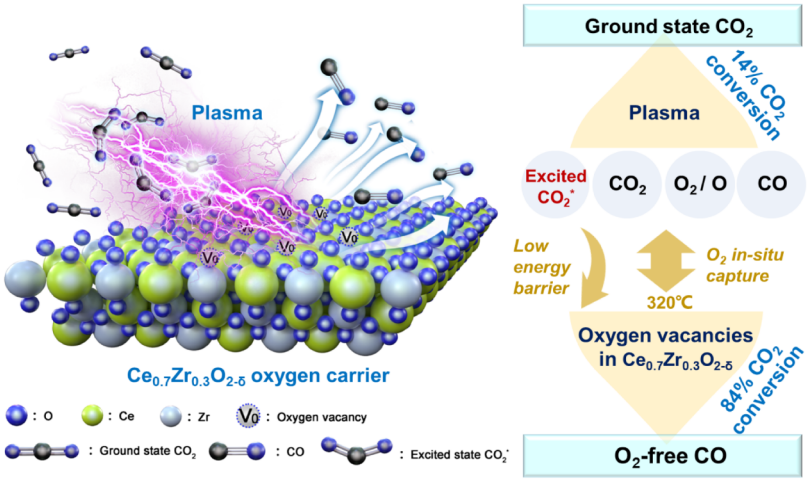

Figure 7. Schematic of the synergy between plasma and $Ce_{0.7}Zr_{0.3}O_{2-\delta}$ in the PCLCS.

partial decomposition of the stable CO_2 molecules, facilitated by energetic electrons and the generated reactive species. This process yields a mixture of CO, O_2, or O and electronically/vibrationally excited CO_2* molecules (besides ground-state CO_2), contributing to a 14% conversion of CO_2. 3) The excited CO_2* then efficiently undergoes splitting over the $Ce_{0.7}Zr_{0.3}O_{2-\delta}$ OC, which possesses abundant oxygen vacancies, exhibiting a substantially reduced activation barrier compared to the ground-state CO_2. Note that this process was proven to be unfeasible for the ground-state CO_2 at 320 °C. 4) The O_2 or O produced by plasma is captured in situ by the oxygen vacancies in $Ce_{0.7}Zr_{0.3}O_{2-\delta}$. We also compared the adsorption energies of O_2/O and CO_2 on the $Ce_{0.75}Zr_{0.25}O_{2-\delta}$ (111) surface, the results of which are summarized in Table S8. Both O_2 and O exhibit higher adsorption energies compared to CO_2. Therefore, there may be competition between O_2/O and CO_2 for oxygen vacancies in the OCs. However, given the relatively low concentration of O_2/O compared to that of CO_2 in the system (e.g., 4.4% CO_2 and 0.3 vol% O_2 after plasma, as measured), the influence of the concentration of O_2/O is expected to be unimportant. This not only significantly contributes to the formation of O_2-free CO but also facilitates the forward progression of the CO_2 decomposition reaction, adhering to Le Chatelier's principle.

The synergistic interaction between plasma and $Ce_{0.7}Zr_{0.3}O_{2-\delta}$ in the PCLCS system achieves a CO_2 conversion of up to 84%, producing the desired O_2-free CO product at a fairly low temperature of 320 °C. Last but not least, plasma can be powered by renewable energy sources and operates in an intermittent and decentralized manner. As a turnkey process, it allows for instant on/off switching and has no economy of scale.

CONCLUSIONS

In this study, we introduce a novel PCLCS system that integrates an RGA plasma with a $Ce_xZr_{1-x}O_2$ OC, enabling efficient conversion of CO_2 into an O_2-free CO at mild temperatures.

Incorporating Zr into CeO_2 substantially enhances the reaction performance by forming a Ce−Zr−O solid solution due to improved oxygen vacancy formation and lattice oxygen mobility, as experimentally and theoretically evidenced. The PCLCS system utilizing $Ce_{0.7}Zr_{0.3}O_{2-\delta}$ achieves a high CO_2 conversion of up to 84% and a CO yield of 1.3 mmol g^{-1}, with no measurable O_2. This exceptional performance is realized at a mild temperature of only 320 °C, highlighting the superiority of the proposed system over traditional thermal CL processes (typically at 650−1000 °C). Furthermore, the achieved conversion surpasses those reported in NTP-based CO_2 splitting processes (only 4%−50%), indicating a robust synergy between plasma and $Ce_{0.7}Zr_{0.3}O_{2-\delta}$.

In PCLCS, plasma initially activates and partially decomposes the stable CO_2 molecules to yield CO, O_2/O, and electronically/vibrationally excited CO_2*, contributing to a 14% conversion of CO_2. Importantly, the excited CO_2* can then efficiently decompose over $Ce_{0.7}Zr_{0.3}O_{2-\delta}$ that possesses abundant oxygen vacancies, exhibiting a substantially reduced activation barrier (0.86 eV) compared to that of the ground-state CO_2 (1.63 eV), as confirmed by DFT calculations. The strong O_2/O capture ability of $Ce_{0.7}Zr_{0.3}O_{2-\delta}$ further accelerates the CO_2 decomposition reactions, facilitating the generation of O_2-free CO.

The proposed PCLCS strategy, which can be powered by renewable electricity in an intermittent and decentralized manner due to the instant on/off switching feature of plasma, is poised to emerge as a viable solution for addressing the grand challenge of conversion of CO_2 to clean CO.

METHODS

Experimental Setup and Methods

The PCLCS setup comprising a custom-built RGA reactor and a quartz cover housing OCs is illustrated in Figure 1 in the manuscript. Detailed configuration of the setup and further information on the experimental system are presented in Figures S1 and S2, respectively. The RGA reactor is composed of a cone-shaped inner anode and a circular cathode. A direct current (DC) power source (Teslaman TLP2040) powered the discharge in series for stabilizing the discharge current. The reactant gas, a mixture of 5 vol% CO_2 diluted with 95 vol% Ar, entered through three tangential inlets at the bottom of the reactor, inducing a swirling flow. The total gas flow rate was controlled at 500 mL min^{-1} using mass flow controllers for both CO_2 and Ar. An annular magnet situated outside the cathode generated an upward magnetic field. The interplay of swirling flow and Lorentz force caused the arc to ascend and finally rotate rapidly around the inner anode, forming a stable plasma "disc" conducive to chemical reactions. More details on the RGA reactor can be found in our previous work.[37,69] Voltage and current signals were measured using Tektronix P6015A and Tektronix TCP303 probes, with waveforms recorded by a Tektronix DPO4034B oscilloscope. The discharge power during experiments was then determined to range from 67.6 to 71.5 W.

As illustrated in Figure 1, a downstream quartz cover (inner diameter: 14 mm) housed the OCs for the second-stage reactions. Each

https://doi.org/10.1021/jacsau.4c00153
JACS Au 2024, 4, 2462−2473

experiment utilized 1 g of 20−40 mesh reduced pellet OCs, positioned approximately 2 mm from the plasma area. The length of the OC bed is approximately 0.6 mm. Note that no additional heating was applied to the reaction area. A thermocouple (type NR-81530K) was positioned in the proximity of the surface of the oxygen carriers to measure the reaction temperature. Before introducing the reactant gas, pure N_2 (99.99%) purged the reactor until the reaction area reached room temperature.

A schematic of the experimental setup is presented in Figure S2. The setup consists of a gas feeding system, a power supply, an RGA reactor with a gas sampling set, and an oscilloscope with high-voltage and current probes for electrical parameter measurement. Effluent gases were continuously monitored using an NDIR gas analyzer (GASBOARD-3100, Wuhan Cubic Optoelectronic Co., Ltd.) and a gas chromatograph (Agilent 7890) equipped with a thermal conductivity detector (TCD) and two capillary columns (HP-PLOT 5A, HP-PLOT-Q).

Plasma CO_2 splitting reaction. The reduced OCs with a size of 20−40 mesh were placed into the plasma reactor (a quartz tube with 14 mm inside diameter), and then, the CO_2 (5 vol% CO_2/Ar) flowed through the reactor for reacting with the OCs. The outlet gases were monitored by an NDIR gas analyzer (GASBOARD-3100, Wuhan Cubic Optoelectronic Co., Ltd.).

Successive PCLCS testing. After the $Ce_xZr_{1-x}O_2$ OC is reduced by H_2 for 1 h, pure N_2 (99.99%) was introduced to purge the reactor instead of the H_2 until the reactor concentration drops to room temperature. Then, the reduced OCs were placed into the plasma reactor for the plasma CO_2 splitting reaction. The outlet gases were monitored by an NDIR gas analyzer (GASBOARD-3100, Wuhan cubic optoelectronic Co., Ltd.).

The effectiveness of PCLCS was evaluated based on CO_2 conversion, CO yield, CO purity in the gas products, and energy efficiency, with calculations performed using the following formulas:

CO_2 conversion:

$$X_{CO_2}(\%) = \frac{C_{CO_2,in} - C_{CO_2,out}}{C_{CO_2,in}} \times 100\% \quad (1)$$

CO yield:

$$y_{CO}\ (\text{mmol}\ g^{-1}) = \frac{\int_0^t C_{CO,out}\ dt \times F}{R \times m_{oxygen\ carrier}} \quad (2)$$

CO purity in the gas products:

$$p_{CO}\ (\%) = \frac{\int_0^t C_{CO,out}\ dt \times F}{\int_0^t C_{CO,out}\ dt \times F + \int_0^t C_{O_2,out}\ dt \times F} \times 100\% \quad (3)$$

energy efficiency:

$$\eta\ (\%) = \frac{F_{CO_2} \times X_{CO_2} \times \Delta H}{60 \times R \times P_d} \times 100\% \quad (4)$$

where C represents the gas concentration, vol%; t signifies time, s; F denotes the gas flow rate, mL min^{-1}; P_d is the plasma discharge power, W; ΔH is the reaction enthalpy of pure CO_2 splitting, 280 kJ mol^{-1}, and R corresponds to the volume of an ideal gas at standard temperature and pressure, 22.4 L mol^{-1}. The value of P_d is 69 W in this work.

Synthesis and Reduction of $Ce_xZr_{1-x}O_2$ Oxygen Carriers

In chemical looping processes, an OC with a high oxygen-carrying capacity is essential for facilitating the transport of energy and oxygen during redox reactions. Cerium-based oxides, such as CeO_2, are recognized for high oxygen anion (O^{2-}) conductivity, making them promising redox OCs.[47] However, maintaining satisfactory O^{2-} conductivity and redox kinetics at relatively low temperatures (e.g., < 800 °C) remains challenging for unmodified CeO_2.[20] The concentration of oxygen vacancies and their energy barrier for migration become crucial at low temperatures, influencing the rate at which lattice oxygen participates in the redox reactions. The fluorite structure, however, provides an avenue to enhance O^{2-} conductivity and/or structural stability by accommodating cation dopants. Among various cations, the tetravalent Zr ion emerges as a suitable candidate due to its size similarity to Ce^{4+}.[61]

In this study, $Ce_{1-x}Zr_xO_2$ OCs, where x = 0.1, 0.2, 0.3, 0.4, and 0.5 in mole fraction, were synthesized for PCLCS experiments, by using the coprecipitation method. In a typical procedure, $Ce(NO_3)_3{\cdot}6H_2O$ and $Zr(NO_3)_4{\cdot}5H_2O$ were dissolved in deionized water, yielding a total cation concentration of 2.0 mol L^{-1}. Subsequently, an 8 wt % ammonia aqueous solution was added dropwise to the mixed solution under continuous stirring until the pH reached 10. The resulting solid−liquid mixture underwent additional stirring for 3 h. After aging at room temperature for 12 h, the mixture was filtered and washed multiple times. The precipitate was subsequently dried at 110 °C for 24 h and calcinated at 800 °C for 2 h to obtain $Ce_xZr_{1-x}O_2$ powder OCs. Finally, the powder OCs were compacted at 10 MPa for 15 min, crushed, and sieved to produce pellet OCs with a particle size ranging from 20 to 40 mesh. The fresh OCs and the oxidized OCs after each PCLCS experiment ($Ce_{1-x}Zr_xO_2$) were reverted to reduced $Ce_{1-x}Zr_xO_{2-\delta}$ in another half cycle using H_2 in a heated fixed-bed reactor at 1 atm. The process involved initial heating in pure N_2 at a temperature ramp of 10 °C min^{-1} from room temperature to 800 °C, followed by reduction under H_2 (10 vol% H_2/N_2) for 1 h.

Material Characterizations

Powder XRD patterns were acquired to investigate the crystallographic phase of OCs using a MiniFlex600 Rigaku XRD meter with Cu Kα radiation (λ= 0.15406 nm). The diffraction patterns were collected under ambient conditions within a 2θ range of 10°−90° with a step size of 2° min^{-1}.

SEM (VERSA 3D, FEI) was employed to examine the morphology of the OCs. The as-prepared samples were sputter coated with a thin layer of gold, and imaging was performed at an electron beam acceleration of 3 kV.

The specific surface area of the OCs was determined using the BET method with a Quantachrome NOVA 2000e instrument, employing volumetric nitrogen adsorption at −196 °C.

TEM was conducted by using a Tecnai G^2 TF30 S-Twin microscope operating at 300 kV. The specimens were crushed into a powder and then immersed in a small volume of ethanol. After sonicating the mixture for 10 min, a droplet of the suspension was allowed to dry on a holey carbon/Formvar-coated copper TEM grid.

XPS experiments were carried out using a Thermo Fisher Scientific K-Alpha$^+$ system equipped with a monochromatic Al-Ka X-rays source. Spectra were recorded under sample purging at ambient temperature in a vacuum (residual pressure of <10^{-7} Pa). An electron flood gun compensated for sample charging during the measurement. The C 1 s signal at 284.8 eV served as an internal standard for calibration of the XPS signals.

H_2-TPR was performed using a Quantanchrome Instrument. After standard cleaning pretreatment, 100 mg of OCs in a U-tube reactor was heated from room temperature to 900 °C with a heating rate of 10 °C min^{-1} in a 10 vol% H_2/Ar flow (25 mL min^{-1}).

CO_2-TPO experiments were carried out on a microreactor system (Hiden Analytical Co.). Fresh samples were reduced in a 10 vol% CO_2/Ar stream at 450 °C for 2 h, cooled to room temperature in pure Ar, and subjected to CO_2 at room temperature for 1 h. Subsequently, the temperature was increased to 600 °C in flowing Ar. Gas compositions were analyzed using online mass spectrometer. Blank measurements on the OCs were also performed to identify contributions for carbonate species present on the OCs before and after CO_2 exposure.

DFT Calculations

Periodic energy calculations were conducted using the DFT approach, implemented in the Vienna Ab-intio Simulation Package (VASP) code.[70] The generalized gradient approximation (GGA) with the Perdew−Burke−Ernzerhof (PBE) equation was adopted to calculate

https://doi.org/10.1021/jacsau.4c00153
JACS Au 2024, 4, 2462−2473

the exchange correlation energy, with core electrons (Ce: $5p^6\ 5d^1\ 4f^1\ 6s^2$; Zr: $4s^2\ 4p^6\ 5s^2\ 5d^2$; O: $2s^2\ 2p^4$) treated using the projected augmented wave (PAW) approximation. The Kohn−Sham equations were solved with a plane wave cutoff energy of 400 eV and a 4 × 4 × 1 k-point grid supported by the Monkhorst−Pack Method, ensuring geometry optimization reached a force convergence threshold lower than 0.02 eV. More details about the selection of the computational parameters could be found in our previous work.[71] All the systems were treated with the DFT+U methodology with a Hubbard parameter "U" of 5.00 eV to well describe the Ce(4f) electrons.[72] Moreover, transition states (TS) involving O-vacancy immigration and the CO_2 dissolution process were identified using a combined method of CI-NEB +DIMER.[73] TS with a single vibrational frequency were emphasized.

The optimization of excited state CO_2* adsorption involved fixing CO_2* at its equilibrium position, while the $Ce_{0.75}Zr_{0.25}O_{2-\delta}$ bulk substrate underwent relaxation. Conversely, for ground-state adsorbate systems, structural relaxation was applied in all cases. The adsorption energy is defined as

$$E_{ads} = E_{adsorbate/substrate} - (E_{adsorbate} + E_{substrate}) \quad (5)$$

Herein, E_{ads} represents the adsorption energy of the intermediate in eV; $E_{adsorbate/substrate}$ denotes the total energy of the entire adsorption system; $E_{adsorbate}$ signifies the energy of the adsorbed molecules in the free state vacuum; and $E_{substrate}$ refers to the energy of the surface system.

The reaction energy E_r and the activation barrier E_b are defined as

$$E_r = E_{FS} - E_{IS} \qquad E_b = E_{TS} - E_{IS} \quad (6)$$

where E_{FS}, E_{IS}, and E_{TS} refer to the total energy of the final state, initial state, and transition state, respectively.

■ ASSOCIATED CONTENT

Supporting Information

The Supporting Information is available free of charge at https://pubs.acs.org/doi/10.1021/jacsau.4c00153.

Additional information on the methods and results of experiments and DFT calculations; summary of the PCLCS experimental results over reduced $Ce_{0.7}Zr_{0.3}O_{2-\delta}$ OCs (Table S1); fresh CeO_2 and $Ce_{0.7}Zr_{0.3}O_2$ lattice parameters and refinement factors (Table S2); computed formation energy of each oxygen vacancy in $Ce_{0.75}Zr_{0.25}O_{2-\delta}$ (Table S3); computed migration barrier of each oxygen migration to O_2 in $Ce_{0.75}Zr_{0.25}O_{2-\delta}$ (Table S4); computed formation energy of each oxygen vacancy in $Ce_{0.75}Zr_{0.25}O_{2-\delta}$ (Table S5); computed migration barrier of each oxygen migration to O_2 in $Ce_{0.75}Zr_{0.25}O_{2-\delta}$ (Table S6); computed migration barrier of each oxygen migration to O_2 in $Ce_{0.75}Zr_{0.25}O_{2-\delta}$ (Table S7); computed adsorption energy of intermediates on $Ce_{0.7}Zr_{0.3}O_2$ (111) surface (Table S8) (PDF)

■ AUTHOR INFORMATION

Corresponding Authors

Hai Zhang − *School of Mechanical Engineering, Shanghai Jiao Tong University, Shanghai 200240, China;* orcid.org/0000-0002-6624-1224; Email: zhanghai@sjtu.edu.cn

Jianhua Yan − *State Key Laboratory of Clean Energy Utilization, Zhejiang University, Hangzhou 310027, China; Ningbo Innovation Center, Zhejiang University, Ningbo 315100, China*; Email: yanjh@zju.edu.cn

Xin Tu − *Department of Electrical Engineering and Electronics, University of Liverpool, Liverpool L69 3GJ, U.K.;* orcid.org/0000-0002-6376-0897; Email: xin.tu@liv.ac.uk

Hao Zhang − *State Key Laboratory of Clean Energy Utilization, Zhejiang University, Hangzhou 310027, China; Ningbo Innovation Center, Zhejiang University, Ningbo 315100, China;* orcid.org/0000-0002-1639-4089; Email: zhang_hao@zju.edu.cn

Authors

Yanhui Long − *State Key Laboratory of Clean Energy Utilization and College of Energy Engineering, ZJU-UIUC, Zhejiang University, Hangzhou 310027, China*

Xingzi Wang − *School of Mechanical Engineering, Shanghai Jiao Tong University, Shanghai 200240, China*

Kaiyi Wang − *State Key Laboratory of Clean Energy Utilization, Zhejiang University, Hangzhou 310027, China*

Wee-Liat Ong − *College of Energy Engineering, ZJU-UIUC, Zhejiang University, Hangzhou 310027, China;* orcid.org/0000-0003-3035-6991

Annemie Bogaerts − *Research Group PLASMANT, Department of Chemistry, University of Antwerp, Antwerp 2610, Belgium;* orcid.org/0000-0001-9875-6460

Kongzhai Li − *State Key Laboratory of Complex Nonferrous Metal Resources Clean Utilization, Kunming University of Science and Technology, Kunming 650093, China*

Chunqiang Lu − *Department of Electrical Engineering and Electronics, University of Liverpool, Liverpool L69 3GJ, U.K.*

Xiaodong Li − *State Key Laboratory of Clean Energy Utilization, Zhejiang University, Hangzhou 310027, China;* orcid.org/0000-0002-5331-5968

Complete contact information is available at: https://pubs.acs.org/10.1021/jacsau.4c00153

Author Contributions

○Y.L and X.W. contribute equally to this work. CRediT: **Yanhui Long** data curation, formal analysis, investigation, methodology, visualization, writing-original draft; **Xingzi Wang** formal analysis, investigation, software, visualization, writing-original draft; **Hai Zhang** funding acquisition, methodology, supervision, visualization, writing-original draft; **Kaiyi Wang** investigation, visualization, writing-original draft; **Wee-Liat Ong** writing-review & editing; **Annemie Bogaerts** investigation, methodology, software, writing-review & editing; **Kongzhai Li** writing-review & editing; **Chunqiang Lu** writing-review & editing; **Xiaodong Li** writing-review & editing; **Jianhua Yan** conceptualization, funding acquisition, project administration, resources, supervision, writing-review & editing; **Xin Tu** conceptualization, funding acquisition, resources, supervision, writing-review & editing; **Hao Zhang** conceptualization, funding acquisition, project administration, resources, supervision, writing-original draft, writing-review & editing.

Notes

The authors declare no competing financial interest.

■ ACKNOWLEDGMENTS

This work was supported by the National Natural Science Foundation of China (No. 52276214), the "Pioneer" and "Leading Goose" R&D Program of Zhejiang Province (No. 2023C03129), and the Zhejiang Province Basic Public Welfare Research Program (No. LY24E060003). X. Tu acknowledges the funding from the European Union's Horizon 2020 research and innovation program under the Marie Sklodowska- Curie grant agreement No. 813393.

REFERENCES

(1) Song, Q.-W.; Ma, R.; Liu, P.; Zhang, K.; He, L.-N. Recent progress in CO_2 conversion into organic chemicals by molecular catalysis. *Green Chem.* **2023**, *25* (17), 6538−6560.

(2) Tan, T. T.; Kong, F. H.; Yin, H. W.; Cook, L. M.; Middel, A.; Yang, S. Q. Carbon dioxide reduction from green roofs: A comprehensive review of processes, factors, and quantitative methods. *Renewable Sustainable Energy Rev.* **2023**, *182*, 113412.

(3) Ulmer, U.; Dingle, T.; Duchesne, P. N.; Morris, R. H.; Tavasoli, A.; Wood, T.; Ozin, G. A. Fundamentals and applications of photocatalytic CO_2 methanation. *Nat. Commun.* **2019**, *10* (1), 3169.

(4) Hepburn, C.; Adlen, E.; Beddington, J.; Carter, E. A.; Fuss, S.; Mac Dowell, N.; Minx, J. C.; Smith, P.; Williams, C. K. The technological and economic prospects for CO_2 utilization and removal. *Nature* **2019**, *575* (7781), 87−97.

(5) Ye, R.-P.; Ding, J.; Gong, W.; Argyle, M. D.; Zhong, Q.; Wang, Y.; Russell, C. K.; Xu, Z.; Russell, A. G.; Li, Q.; et al. CO_2 hydrogenation to high-value products via heterogeneous catalysis. *Nat. Commun.* **2019**, *10* (1), 5698.

(6) Delikonstantis, E.; Scapinello, M.; Singh, V.; Poelman, H.; Montesano, C.; Martini, L. M.; Tosi, P.; Marin, G. B.; Van Geem, K. M.; Galvita, V. V.; et al. Exceeding Equilibrium CO_2 Conversion by Plasma-Assisted Chemical Looping. *ACS Energy Lett.* **2022**, *7* (6), 1896−1902.

(7) Wang, L.; Du, X.; Yi, Y.; Wang, H.; Gul, M.; Zhu, Y.; Tu, X. Plasma-enhanced direct conversion of CO_2 to CO over oxygen-deficient Mo-doped CeO_2. *Chem. Commun.* **2020**, *56* (94), 14801−14804.

(8) George, A.; Shen, B.; Craven, M.; Wang, Y.; Kang, D.; Wu, C.; Tu, X. A Review of Non-Thermal Plasma Technology: A novel solution for CO_2 conversion and utilization. *Renewable Sustainable Energy Rev.* **2021**, *135*, 109702.

(9) Biswas, A. N.; Winter, L. R.; Xie, Z.; Chen, J. G. Utilizing CO_2 as a Reactant for C3 Oxygenate Production via Tandem Reactions. *JACS Au* **2023**, *3* (2), 293−305.

(10) Wang, Z. J.; Song, H.; Liu, H.; Ye, J. Coupling of Solar Energy and Thermal Energy for Carbon Dioxide Reduction: Status and Prospects. *Angew. Chem., Int. Ed.* **2020**, *59* (21), 8016−8035.

(11) Zhang, H.; Tan, Q.; Huang, Q.; Wang, K.; Tu, X.; Zhao, X.; Wu, C.; Yan, J.; Li, X. Boosting the Conversion of CO_2 with Biochar to Clean CO in an Atmospheric Plasmatron: A Synergy of Plasma Chemistry and Thermochemistry. *ACS Sustainable Chem. Eng.* **2022**, *10* (23), 7712−7725.

(12) Snoeckx, R.; Bogaerts, A. Plasma technology − a novel solution for CO_2 conversion? *Chem. Soc. Rev.* **2017**, *46* (19), 5805−5863.

(13) She, X.; Wang, Y.; Xu, H.; Chi Edman Tsang, S.; Ping Lau, S. Challenges and Opportunities in Electrocatalytic CO_2 Reduction to Chemicals and Fuels. *Angew. Chem., Int. Ed.* **2022**, *61* (49), No. e202211396.

(14) Liu, L.; Dai, J.; Das, S.; Wang, Y.; Yu, H.; Xi, S.; Zhang, Z.; Tu, X. Plasma-Catalytic CO_2 Reforming of Toluene over Hydrotalcite-Derived NiFe/(Mg, Al)O_x Catalysts. *JACS Au* **2023**, *3* (3), 785−800.

(15) Liu, L.; Hu, J.; Ma, Z.; Zhu, Z.; He, B.; Chen, F.; Lu, Y.; Xu, R.; Zhang, Y.; Ma, T.; et al. One-dimensional single atom arrays on ferroelectric nanosheets for enhanced CO_2 photoreduction. *Nat. Commun.* **2024**, *15* (1), 305.

(16) Oughli, A. A.; Ruff, A.; Boralugodage, N. P.; Rodríguez-Maciá, P.; Plumeré, N.; Lubitz, W.; Shaw, W. J.; Schuhmann, W.; Rüdiger, O. Dual properties of a hydrogen oxidation Ni-catalyst entrapped within a polymer promote self-defense against oxygen. *Nat. Commun.* **2018**, *9* (1), 864.

(17) Sholl, D. S.; Lively, R. P. Seven chemical separations to change the world. *Nature* **2016**, *532* (7600), 435−437.

(18) Zhang, X.; Liu, R.; Liu, T.; Pei, C.; Gong, J. Redox catalysts for chemical looping methane conversion. *Trends Chem.* **2023**, *5* (7), 512−525.

(19) Zheng, Y.; Li, K.; Wang, H.; Wang, Y.; Tian, D.; Wei, Y.; Zhu, X.; Zeng, C.; Luo, Y. Structure dependence and reaction mechanism of CO oxidation: A model study on macroporous CeO_2 and CeO_2-ZrO_2 catalysts. *J. Catal.* **2016**, *344*, 365−377.

(20) Haribal, V. P.; Wang, X.; Dudek, R.; Paulus, C.; Turk, B.; Gupta, R.; Li, F. Modified Ceria for "Low-Temperature" CO_2 Utilization: A Chemical Looping Route to Exploit Industrial Waste Heat. *Adv. Energy Mater.* **2019**, *9* (41), 1901963.

(21) Tang, M.; Liu, K.; Roddick, D. M.; Fan, M. Enhanced lattice oxygen reactivity over Fe_2O_3/Al_2O_3 redox catalyst for chemical-looping dry (CO_2) reforming of CH_4: Synergistic La-Ce effect. *J. Catal.* **2018**, *368*, 38−52.

(22) Zheng, Y. E.; Liao, X.; Xiao, H.; Haribal, V.; Shi, X.; Huang, Z.; Zhu, L.; Li, K.; Li, F.; Wang, H.; et al. Highly efficient reduction of O_2-containing CO_2 via chemical looping based on perovskite nanocomposites. *Nano Energy* **2020**, *78*, 105320.

(23) Zhang, X.; Pei, C.; Chang, X.; Chen, S.; Liu, R.; Zhao, Z.-J.; Mu, R.; Gong, J. FeO6 Octahedral Distortion Activates Lattice Oxygen in Perovskite Ferrite for Methane Partial Oxidation Coupled with CO_2 Splitting. *J. Am. Chem. Soc.* **2020**, *142* (26), 11540−11549.

(24) Donat, F.; Müller, C. R. CO_2-free conversion of CH_4 to syngas using chemical looping. *Appl. Catal., B* **2020**, *278*, 119328.

(25) Xia, X.; Chang, W.; Cheng, S.; Huang, C.; Hu, Y.; Xu, W.; Zhang, L.; Jiang, B.; Sun, Z.; Zhu, Y.; et al. Oxygen Activity Tuning via FeO_6 Octahedral Tilting in Perovskite Ferrites for Chemical Looping Dry Reforming of Methane. *ACS Catal.* **2022**, *12* (12), 7326−7335.

(26) Zhang, J.; Haribal, V.; Li, F. Perovskite nanocomposites as effective CO_2-splitting agents in a cyclic redox scheme. *Sci. Adv.* **2017**, *3* (8), No. e1701184.

(27) Wu, P.; Li, X.; Ullah, N.; Li, Z. Synergistic effect of catalyst and plasma on CO_2 decomposition in a dielectric barrier discharge plasma reactor. *Mol. Catal.* **2021**, *499*, 111304.

(28) Uytdenhouwen, Y.; Meynen, V.; Cool, P.; Bogaerts, A. The Potential Use of Core-Shell Structured Spheres in a Packed-Bed DBD Plasma Reactor for CO_2 Conversion. *Catalysts* **2020**, *10*, 530.

(29) Zhang, K.; Harvey, A. P. CO_2 decomposition to CO in the presence of up to 50% O_2 using a non-thermal plasma at atmospheric temperature and pressure. *Chem. Eng. J.* **2021**, *405*, 126625.

(30) Uytdenhouwen, Y.; Van Alphen, S.; Michielsen, I.; Meynen, V.; Cool, P.; Bogaerts, A. A packed-bed DBD micro plasma reactor for CO_2 dissociation: Does size matter? *Chem. Eng. J.* **2018**, *348*, 557−568.

(31) Xia, M.; Ding, W.; Shen, C.; Zhang, Z.; Liu, C.-J. CeO_2-Enhanced CO_2 Decomposition via Frosted Dielectric Barrier Discharge Plasma. *Ind. Eng. Chem. Res.* **2022**, *61* (29), 10455−10460.

(32) Mei, D.; Tu, X. Atmospheric Pressure Non-Thermal Plasma Activation of CO_2 in a Packed-Bed Dielectric Barrier Discharge Reactor. *ChemPhyschem* **2017**, *18* (22), 3253−3259.

(33) Mei, D.; Zhu, X.; Wu, C.; Ashford, B.; Williams, P. T.; Tu, X. Plasma-photocatalytic conversion of CO_2 at low temperatures: Understanding the synergistic effect of plasma-catalysis. *Appl. Catal., B* **2016**, *182*, 525−532.

(34) Mei, D.; He, Y.-L.; Liu, S.; Yan, J.; Tu, X. Optimization of CO_2 Conversion in a Cylindrical Dielectric Barrier Discharge Reactor Using Design of Experiments. *Plasma Processes Polym.* **2016**, *13* (5), 544−556.

(35) Paulussen, S.; Verheyde, B.; Tu, X.; De Bie, C.; Martens, T.; Petrovic, D.; Bogaerts, A.; Sels, B. Conversion of carbon dioxide to value-added chemicals in atmospheric pressure dielectric barrier discharges. *Plasma Sources Sci. Technol.* **2010**, *19* (3), 034015.

(36) Li, L.; Zhang, H.; Li, X.; Kong, X.; Xu, R.; Tay, K.; Tu, X. Plasma-assisted CO_2 conversion in a gliding arc discharge: Improving performance by optimizing the reactor design. *J. CO2 Util.* **2019**, *29*, 296−303.

(37) Zhang, H.; Li, L.; Li, X.; Wang, W.; Yan, J.; Tu, X. Warm plasma activation of CO_2 in a rotating gliding arc discharge reactor. *J. CO2 Util.* **2018**, *27*, 472−479.

(38) Renninger, S.; Lambarth, M.; Birke, K. P. High efficiency CO_2-splitting in atmospheric pressure glow discharge. *J. CO2 Util.* **2020**, *42*, 101322.

(39) Renninger, S.; Stein, J.; Lambarth, M.; Birke, K. P. An optimized reactor for CO_2 splitting in DC atmospheric pressure discharge. *J. CO2 Util.* **2022**, *58*, 101919.

https://doi.org/10.1021/jacsau.4c00153
JACS Au 2024, 4, 2462−2473

(40) Indarto, A.; Yang, D. R.; Choi, J.-W.; Lee, H.; Song, H. K. Gliding arc plasma processing of CO_2 conversion. *J. Hazard. Mater.* **2007**, *146* (1), 309−315.
(41) Nunnally, T.; Gutsol, K.; Rabinovich, A.; Fridman, A.; Gutsol, A.; Kemoun, A. Dissociation of CO_2 in a low current gliding arc plasmatron. *J. Phys. D: Appl. Phys.* **2011**, *44* (27), 274009.
(42) Liu, J.-L.; Park, H.-W.; Chung, W.-J.; Park, D.-W. High-Efficient Conversion of CO_2 in AC-Pulsed Tornado Gliding Arc Plasma. *Plasma Chem. Plasma Process.* **2016**, *36* (2), 437−449.
(43) Spencer, L. F.; Gallimore, A. D. CO_2 dissociation in an atmospheric pressure plasma/catalyst system: a study of efficiency. *Plasma Sources Sci. Technol.* **2013**, *22* (1), 015019.
(44) Bak, M. S.; Im, S. K.; Cappelli, M. Nanosecond-pulsed discharge plasma splitting of carbon dioxide. *IEEE Trans. Plasma Sci.* **2015**, *43* (4), 1002−1007.
(45) Moss, M. S.; Yanallah, K.; Allen, R. W. K.; Pontiga, F. An investigation of CO_2 splitting using nanosecond pulsed corona discharge: Effect of argon addition on CO_2 conversion and energy efficiency. *Plasma Sources Sci. Technol.* **2017**, *26* (3), 035009.
(46) Zhang, X.; Liu, Y.; Zhang, M.; Yu, T.; Chen, B.; Xu, Y.; Crocker, M.; Zhu, X.; Zhu, Y.; Wang, R.; et al. Synergy between β-Mo_2C Nanorods and Non-thermal Plasma for Selective CO_2 Reduction to CO. *Chem* **2020**, *6* (12), 3312−3328.
(47) Ruan, C.; Huang, Z.-Q.; Lin, J.; Li, L.; Liu, X.; Tian, M.; Huang, C.; Chang, C.-R.; Li, J.; Wang, X. Synergy of the catalytic activation on Ni and the CeO_2−TiO_2/$Ce_2Ti_2O_7$ stoichiometric redox cycle for dramatically enhanced solar fuel production. *Energy Environ. Sci.* **2019**, *12* (2), 767−779.
(48) Löfberg, A.; Guerrero-Caballero, J.; Kane, T.; Rubbens, A.; Jalowiecki-Duhamel, L. Ni/CeO_2 based catalysts as oxygen vectors for the chemical looping dry reforming of methane for syngas production. *Appl. Catal., B* **2017**, *212*, 159−174.
(49) Rocchini, E.; Trovarelli, A.; Llorca, J.; Graham, G. W.; Weber, W. H.; Maciejewski, M.; Baiker, A. Relationships between Structural/Morphological Modifications and Oxygen Storage−Redox Behavior of Silica-Doped Ceria. *J. Catal.* **2000**, *194* (2), 461−478.
(50) Zheng, Y.; Li, K.; Wang, H.; Zhu, X.; Wei, Y.; Zheng, M.; Wang, Y. Enhanced Activity of CeO_2−ZrO_2 Solid Solutions for Chemical-Looping Reforming of Methane via Tuning the Macroporous Structure. *Energy Fuels* **2016**, *30* (1), 638−647.
(51) Markaryan, G. L.; Ikryannikova, L. N.; Muravieva, G. P.; Turakulova, A. O.; Kostyuk, B. G.; Lunina, E. V.; Lunin, V. V.; Zhilinskaya, E.; Aboukais, A. Red−ox properties and phase composition of CeO_2−ZrO_2 and Y_2O_3−CeO_2−ZrO_2 solid solutions. *Colloids Surf., A* **1999**, *151* (3), 435−447.
(52) Liu, H.-X.; Li, S.-Q.; Wang, W.-W.; Yu, W.-Z.; Zhang, W.-J.; Ma, C.; Jia, C.-J. Partially sintered copper−ceria as excellent catalyst for the high-temperature reverse water gas shift reaction. *Nat. Commun.* **2022**, *13* (1), 867.
(53) Hu, B.; Sun, K.; Zhuang, Z.; Chen, Z.; Liu, S.; Cheong, W.-C.; Chen, C.; Hu, M.; Cao, X.; Ma, J.; et al. Distinct Crystal-Facet-Dependent Behaviors for Single-Atom Palladium-On-Ceria Catalysts: Enhanced Stabilization and Catalytic Properties. *Adv. Mater.* **2022**, *34* (16), 2107721.
(54) Zheng, Y.; Li, K.; Wang, H.; Tian, D.; Wang, Y.; Zhu, X.; Wei, Y.; Zheng, M.; Luo, Y. Designed oxygen carriers from macroporous $LaFeO_3$ supported CeO_2 for chemical-looping reforming of methane. *Appl. Catal., B* **2017**, *202*, 51−63.
(55) Ao, X.; Wang, H.; Wei, Y. Novel method for metallic zinc and synthesis gas production in alkali molten carbonates. *Energy Convers. Manage.* **2008**, *49* (8), 2063−2068.
(56) Long, Y.; Yang, K.; Gu, Z.; Lin, S.; Li, D.; Zhu, X.; Wang, H.; Li, K. Hydrogen generation from water splitting over polyfunctional perovskite oxygen carriers by using coke oven gas as reducing agent. *Appl. Catal., B* **2022**, *301*, 120778.
(57) Li, D.; Xu, R.; Li, X.; Li, Z.; Zhu, X.; Li, K. Chemical Looping Conversion of Gaseous and Liquid Fuels for Chemical Production: A Review. *Energy Fuels* **2020**, *34* (5), 5381−5413.
(58) Yang, Z.; Luo, G.; Lu, Z.; Hermansson, K. Oxygen vacancy formation energy in Pd-doped ceria: A DFT+U study. *J. Chem. Phys.* **2007**, *127*, 074704.
(59) Zhang, L.; Meng, J.; Yao, F.; Zhang, W.; Liu, X.; Meng, J.; Zhang, H. Insight into the Mechanism of the Ionic Conductivity for Ln-Doped Ceria (Ln = La, Pr, Nd, Pm, Sm, Gd, Tb, Dy, Ho, Er, and Tm) through First-Principles Calculation. *Inorg. Chem.* **2018**, *57* (20), 12690−12696.
(60) Li, H. Y.; Wang, H. F.; Guo, Y. L.; Lu, G. Z.; Hu, P. Exchange between sub-surface and surface oxygen vacancies on CeO_2(111): A new surface diffusion mechanism. *Chem. Commun.* **2011**, *47* (21), 6105−6107.
(61) Zheng, Y.; Wei, Y.; Li, K.; Zhu, X.; Wang, H.; Wang, Y. Chemical-looping steam methane reforming over macroporous CeO_2−ZrO_2 solid solution: Effect of calcination temperature. *Int. J. Hydrogen Energy* **2014**, *39* (25), 13361−13368.
(62) Kim, D.-Y.; Ham, H.; Chen, X.; Liu, S.; Xu, H.; Lu, B.; Furukawa, S.; Kim, H.-H.; Takakusagi, S.; Sasaki, K.; et al. Cooperative Catalysis of Vibrationally Excited CO_2 and Alloy Catalyst Breaks the Thermodynamic Equilibrium Limitation. *J. Am. Chem. Soc.* **2022**, *144* (31), 14140−14149.
(63) Yan, X.; Zhao, B.; Liu, Y.; Li, Y. Dielectric barrier discharge plasma for preparation of Ni-based catalysts with enhanced coke resistance: Current status and perspective. *Catal. Today* **2015**, *256*, 29−40.
(64) https://www.bolsig.laplace.univ-tlse.fr/index.html.
(65) Fu, P.; Huang, M.; Shang, Y.; Yu, N.; Zhou, H.-L.; Zhang, Y.-B.; Chen, S.; Gong, J.; Ning, Z. Organic−Inorganic Layered and Hollow Tin Bromide Perovskite with Tunable Broadband Emission. *ACS Appl. Mater. Interfaces* **2018**, *10* (40), 34363−34369.
(66) Saito, N.; Muramatsu, Y.; Chiba, H.; Ueda, K.; Kubozuka, K.; Koyano, I.; Okada, K.; Jagutzki, O.; Czasch, A.; Weber, T.; et al. Deformation, nuclear motion and fragmentation of core-excited CO_2 probed by multiple-ion coincidence momentum imaging. *J. Electron Spectrosc. Relat. Phenom.* **2004**, *141* (2−3), 183−193.
(67) El-Gammal, O. A.; Rakha, T. H.; Metwally, H. M.; Abu El-Reash, G. M. Synthesis, characterization, DFT and biological studies of isatinpicolinohydrazone and its Zn(II), Cd(II) and Hg(II) complexes. *Spectrochim. Acta, Part A* **2014**, *127*, 144−156.
(68) Calvaresi, M.; Martinez, R. V.; Losilla, N. S.; Martinez, J.; Garcia, R.; Zerbetto, F. Splitting CO_2 with Electric Fields: A Computational Investigation. *J. Phys. Chem. Lett.* **2010**, *1* (22), 3256−3260.
(69) Zhang, H.; Wang, W.; Li, X.; Han, L.; Yan, M.; Zhong, Y.; Tu, X. Plasma activation of methane for hydrogen production in a N_2 rotating gliding arc warm plasma: A chemical kinetics study. *Chem. Eng. J.* **2018**, *345*, 67−78.
(70) Hafner, J. Ab-initio simulations of materials using VASP: Density-functional theory and beyond. *J. Comput. Chem.* **2008**, *29* (13), 2044−2078.
(71) Qin, H.; Wang, K.; Zhang, H.; Wang, X.; Wu, J. Understanding the effects of cluster restructuring on water gas shift reaction over Cu/TM (TM = Cu, Ni and Pt) under high concentration of CO. *Appl. Surf. Sci.* **2023**, *613*, 155954.
(72) Lutfalla, S.; Shapovalov, V.; Bell, A. T. Calibration of the DFT/GGA+U Method for Determination of Reduction Energies for Transition and Rare Earth Metal Oxides of Ti, V, Mo, and Ce. *J. Chem. Theory Comput.* **2011**, *7* (7), 2218−2223.
(73) Klimeš, J.; Bowler, D. R.; Michaelides, A. A critical assessment of theoretical methods for finding reaction pathways and transition states of surface processes. *J. Phys.: Condens. Matter* **2010**, *22* (7), 074203.

https://doi.org/10.1021/jacsau.4c00153
JACS Au 2024, 4, 2462−2473